



OPEN

Ultra-wideband, wide angle, asymmetric transmission based chiral metasurface for C and X band applications

Syed Hussain Ali Bokhari & Hammad M. Cheema

A multi-layered chiral device manifesting asymmetric transmission (AT) facilitating one-way channeling of electromagnetic (EM) waves, based on the inherent polarization is presented. The designed metasurface depicts a high transmission contrast with an efficiency above 80% for an ultra-wide operational range of 6.3–12.3 GHz, constituting a fractional bandwidth of 64%. As an additional feature, the reported metasurface yields robustness against oblique incidences up to 45° while maintaining high transmission efficiency. This report also introduces a unique analogy of the AT based communication system with logic-gates by formulating its truth-table and logic circuit. Furthermore, new insights of AT magnitude's dependence to oblique incidences are presented on the account of surface impedance mismatch due to TE and TM polarization with varying incidence angle. Moreover, avoidance of grating lobes and the associated transmission deterioration through utilization of electrically small periodic metasurface is presented. The results have been numerically and practically validated yielding state-of-the-art features. Operating within C and X band, the reported work is an ideal candidate for practical AT applications.

Controlling the flow of electromagnetic (EM) waves has long been intriguing to researchers. The fascination to manipulate EM light has given rise to a number of functionalities such as cross-polarization conversion, EM wave absorption, transmission and reflection etc^{1–7}. Amidst these wave operations, it was deemed most challenging to obtain a directional control of EM waves i.e. allowing light to pass in one direction while blocking it in the other⁸. Non-reciprocal devices that took advantage of inherent gyrotropy in some materials were firstly proposed⁹ and required an external magnetic field for the breakage of time reversal symmetry. The need of an external influence made them bulky and hence inapt for low profile optical systems. Non reciprocal metamaterials and metasurfaces were then tailored to obtain the same functionality¹⁰, however the proposed devices generally suffered from losses due to non-linearities and design complexities.

In comparison, Asymmetric Transmission (AT), a phenomenon firstly discovered by Fedotov in 2006¹¹ allows manipulation of EM wave direction while remaining in a reciprocal regime. The reciprocity, in fact facilitates the engineering of simple and efficient devices. Conceptually, when an AT device encounters a TM wave (x-polarized) in -z-direction, it is transmitted as a TE wave (y-polarized). However, a TE wave incident in same direction undergoes high amount of reflection and is not transmitted. Contrarily, behavior of device becomes opposite for the case of illumination from opposite direction i.e. the AT device becomes transparent for TE wave in +z-direction while blocks the TM wave in the same direction. It can thus be observed that the AT device offers different response in the two directions depending upon the incident polarization of light. Since the inception of AT phenomenon, many effective design topologies have been published. This includes efficient bi-layered configurations^{12–23} and tri-layered configurations as well, which take advantage of Fabry Perot-like cavity thereby resulting in broadband AT response^{24–30}.

The AT phenomenon has been understood through various analogies in the past including electrical models³¹ and physical analyses^{12,32}. Adopting a different approach, this paper introduces a new and interesting analogy based on logic-gates to gain deeper insights. Shown in Fig. 1, consider a full/half-duplex communication system having three input entities; Rx/Tx Antenna 1, Tx/Rx Antenna 2 & an AT device between them. Each of these can be characterized by two states 0/1 corresponding to the antenna polarization (TM/TE) and direction of communication (A1 to A2/ A2 to A1). Likewise, the output of such a system can also be characterized as 0/1

Research Institute for Microwave and Millimeter-Wave Studies (RIMMS), National University of Sciences and Technology (NUST), Islamabad 44000, Pakistan. email: hammad.cheema@rimms.nust.edu.pk

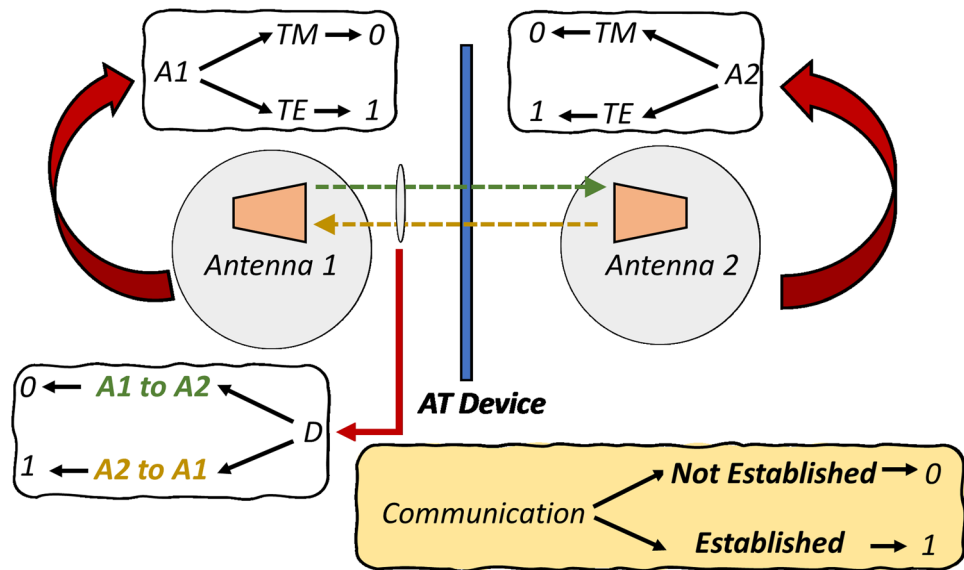


Figure 1. Modeling of logic gates analogy of AT operation.

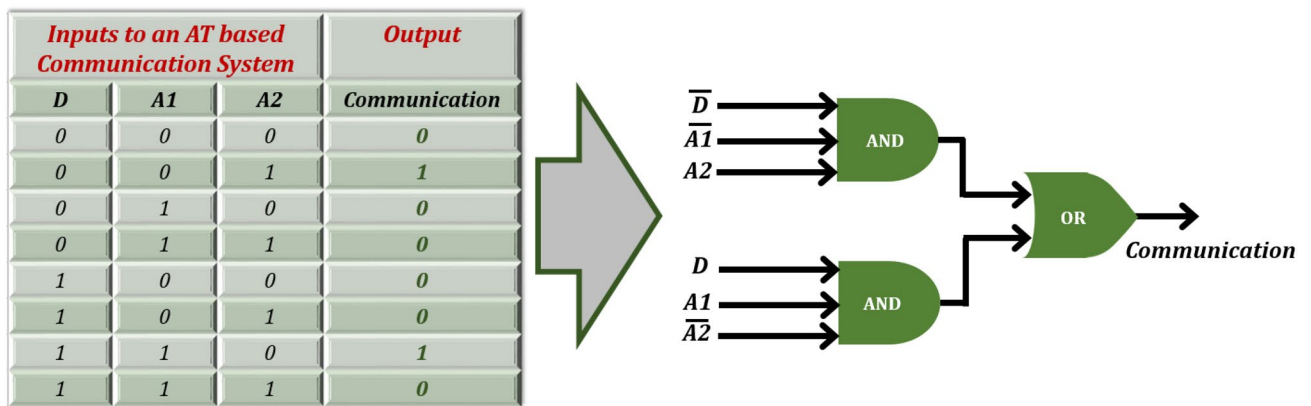


Figure 2. Truth table formulated for the logic gate analogy of AT operation.

depending upon whether a communication channel has been established or not. Next, based on the behavior of a generic AT device, a truth table is devised as shown in Fig. 2. For instance, when both the antennas are of same polarization, no communication is established regardless of direction. However, when the antennas are of different polarization, the establishment of communication becomes dependent on the direction. The formulated table is then processed to form a logic circuit that is fundamentally an OR operation with input being fed from two AND gates whose three inputs D, A1 and A2 are complementary to one another, such that only one of the AND gates can contribute towards enabling the communication channel. It is evident that by switching the direction input to the system, one can control the flow of information between the two antennas. In other words, the communication system becomes direction dependent with respect to the type of polarization incident on the AT device. Such a combinational logic can be utilized as polarization-based control for various modern optical communication applications.

Robustness of any optical device against oblique incidences is an important feature. However, majority of published works have reported device operation at normal incidences alone that generally limits their functionality in practical environments. For instance³³, presents operation at higher incident angles by the use of PIN diodes thereby making it complex to fabricate. Likewise³⁴, only discusses angle of incidence as an extrinsic parameter to tune the structure's performance³², though ensures robust operation up to 30°, however its magnitude decreases at higher incidences^{35,36} present angularly robust AT devices, however they are severely limited in terms of bandwidth. Authors in their recent work³¹ have also proposed a bi-layered AT device that manifests angular performance up to 60°, however, its bandwidth though broad, can still be improved to incorporate multi-band operations.

This paper presents a multi-layered chiral device that mimics a Fabry-perot-like cavity resulting in an ultra-broadband AT operation ranging from 6.3 to 12.3 GHz (fractional bandwidth of 64%) with more than 80%

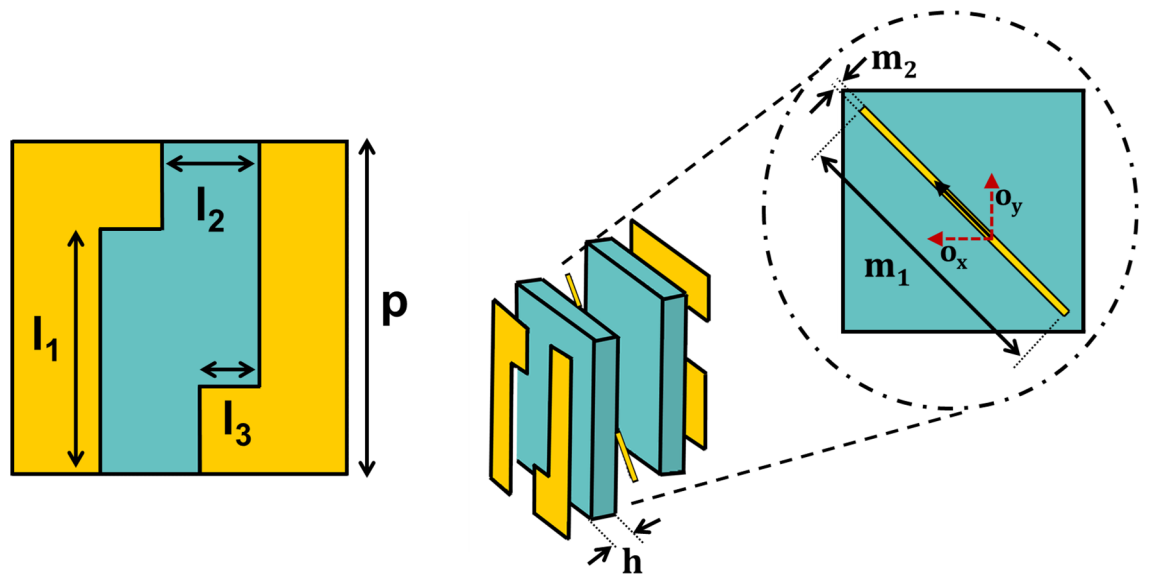


Figure 3. Geometry of the unit cell: $p = 8.35$ mm, $l_1 = 6.15$ mm, $l_2 = 2.43$ mm, $l_3 = 1.52$ mm, $h = 1.16$ mm, $m_1 = 10$ mm, $m_2 = 0.25$ mm Rogers 4725]XR dielectric ($\epsilon = 2.64$, copper cladding = $35 \mu\text{m}$).

transmission efficiency and up to 45° angular stability. Furthermore, the dependence of AT magnitude on impedance mismatch with varying incident angles is studied for the first time thereby explaining the inherent sensitivity of AT to oblique incidences. It is also shown that deterioration by grating lobes can be avoided through careful study and design of the miniaturized unit cell.

Results

Design of multilayered unit-cell for chiral metasurface. Figure 3 illustrates the unit-cell design comprising of three metallic layers sandwiched together by two dielectric substrates and a prepreg, forming a multilayered structure. The top and bottom metallic layers are 90° rotated and mirrored versions of each other and resemble strip-like unit cell design that is similar to³¹. The middle layer constitutes a metallic cut-wire resonator which is rotated at 45° so that an incident wave can cause a dipolar oscillation along its main axis whose orthogonal components (o_x and o_y) can interact and thus contribute towards the polarization conversion phenomena³⁷. Furthermore, two-fold rotational symmetry of the unit cell breaks symmetry in propagation direction thereby ensuring ($T_{xx} = T_{yy}$ and $T_{yx} \neq T_{xy}$). These are the two conditions which are necessary for asymmetric transmission to occur for linearly polarized waves^{38,39}.

The working mechanism of the three metallic layers is explained as follows:

1. The top metallic layer, from the view-point of an array resembles a vertical metallic grating that fundamentally acts as a polarization selector for TM (x-polarization) waves. In other words, an electric field oriented in x-direction will suffer no hindrance by the vertical grating and will pass through. An incident y polarized wave, on the other hand will suffer high reflection since its electric field would be tangential to vertical metal gratings.
2. The bottom metal layer resembles a horizontal grating and therefore acts as a polarization selector for TE (y-polarization) waves. An incident y-polarized wave is selected while an x-polarization is completely reflected. The top and bottom layers, together act as orthogonal gratings that aid in the cross polarization conversion (CPC) phenomenon.
3. The middle metal acts as partially reflective/transmittive layer that interacts with both types of polarizations and aids in producing internal reflections in the structure. The middle layer together with top and bottom gratings results in Fabry-Perot-like cavity that is explained later in the subsection “Fabry-Perot-Like Resonance in the Tri-layered Structure”.

The phenomenon of AT stems from the electromagnetic cross coupling that occurs within a structure and can be mathematically expressed by a parameter known as chirality (κ)⁴⁰. Since, the proposed structure lacks planes of mirror symmetry, it presents a chiral media to the incident EM fields which is governed by the following constitutive relation⁴¹:

$$\begin{bmatrix} D \\ B \end{bmatrix} = \begin{bmatrix} \epsilon & -\frac{j\kappa}{c} \\ \frac{j\kappa}{c} & \mu \end{bmatrix} \begin{bmatrix} E \\ H \end{bmatrix} \quad (1)$$

(κ), in the above equation, quantifies the extent of electromagnetic cross coupling in a structure and can be extracted through the following parameter retrieval equations^{14,42–44}:

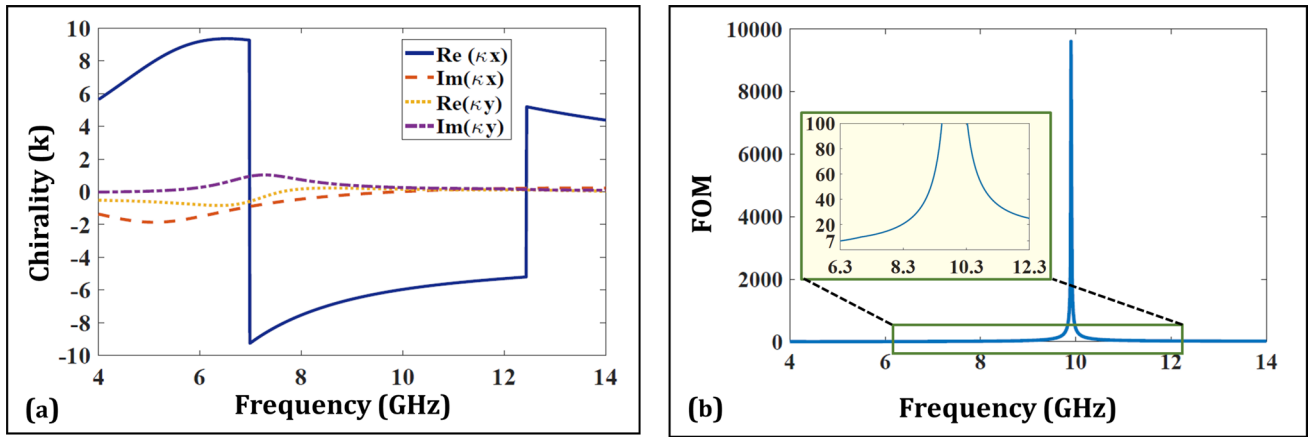


Figure 4. (a) Plotted chirality parameter for the structure. (b) Plotted FOM on chirality parameter.

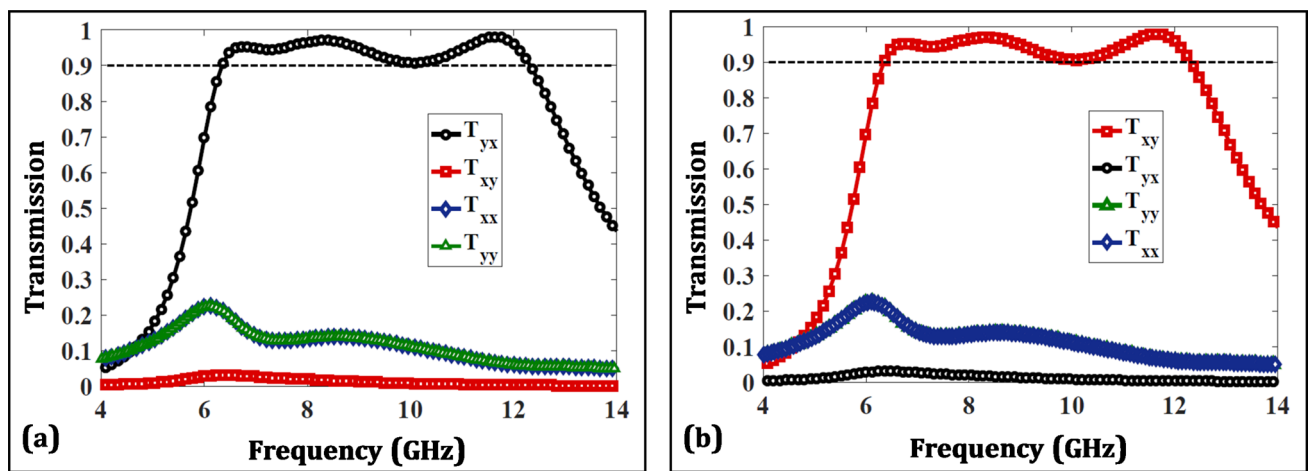


Figure 5. Transmission parameters (a) -z-direction (b) +z-direction.

$$Re(\kappa^{x,y}) = \frac{arg(T_+^{x,y}) - arg(T_-^{x,y})}{2k_0h} \tag{2}$$

$$Im(\kappa^{x,y}) = \frac{\ln |T_-^{x,y}| - \ln |T_+^{x,y}|}{2k_0h} \tag{3}$$

where, h and k_0 are the structure thickness and wave number respectively while $T_{\pm}^x = T_{xx} \mp jT_{yx}$ and $T_{\pm}^y = T_{yy} \pm jT_{xy}$. Figure 4 plots this parameter for the proposed multi-layered chiral structure. It can be observed that the real part of chirality remains greater than 5 in the operating band of interest which denotes higher cross coupling of EM fields. In order to further quantify the quality of chirality in the structure, its figure of merit (FOM = $Re(\kappa) / Im(\kappa)$) is also plotted that shows significant value of greater than 7 in the whole band⁴⁵.

Analysis of scattering parameters. Asymmetric transmission can also be expressed as the difference between transmission coefficients T_{yx} and T_{xy} as given below²⁷:

$$\Delta^x = |T_{yx}|^2 - |T_{xy}|^2 = -\Delta^y \tag{4}$$

It is evident from the above equation that the magnitude of AT is directly influenced by the above difference. The transmission behavior is further elaborated through the well-known Jones Calculus as below:

$$\begin{bmatrix} T_x \\ T_y \end{bmatrix} = \begin{bmatrix} T_{xx} & T_{xy} \\ T_{yx} & T_{yy} \end{bmatrix}^{\pm z} \begin{bmatrix} I_x \\ I_y \end{bmatrix} = T^{\pm z} \begin{bmatrix} I_x \\ I_y \end{bmatrix} \tag{5}$$

where I_x and I_y denote the incident EM wave while T_x and T_y represent the transmitted wave after interacting with the matrix. Figure 5 illustrates the transmission parameters for the proposed multi-layered chiral structure simulated in CST Microwave Studio. It can be seen that when the structure is excited from -z-direction, it passes an incident x-polarized wave as converted y-polarized one while a y-polarized wave impinging in same direction

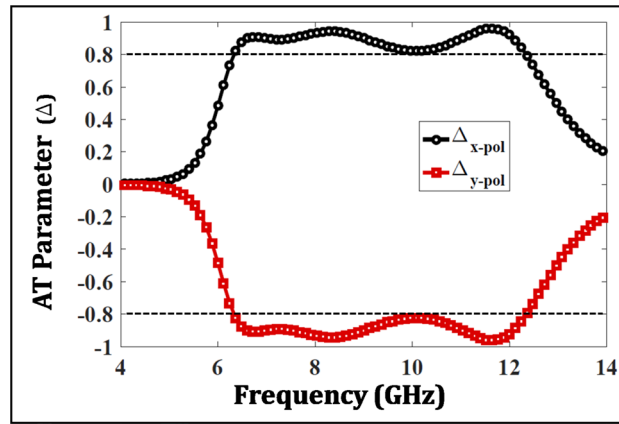


Figure 6. Asymmetric transmission parameter.

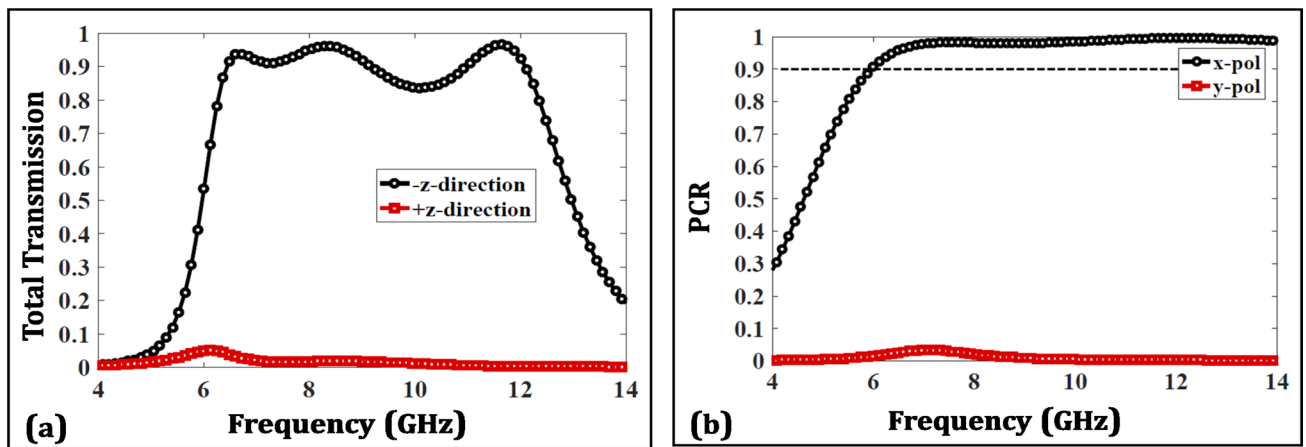


Figure 7. (a) Total transmission. (b) Polarization conversion ratio (PCR).

is transmitted negligibly. This is represented by the coefficient T_{yx} that also reveals a broadband response of 6.3–12.3 GHz above 0.9 magnitude constituting a bandwidth of 64% and exhibiting three peaks reaching 0.95, 0.97 and 0.98 at 6.7, 8.3 and 11.6 GHz, respectively. T_{xy} , $T_{xx} = T_{yy}$ on the other hand remain negligible in the operating band resulting in enhanced AT.

Moreover, it can be observed in Fig. 5b that the two cross polarized coefficients swap their magnitudes when the structure is excited in the +z-direction. For instance, at 11.6 GHz, the T matrix is:

$$T_{11.6GHz} = \begin{bmatrix} 0.067 & 0.004 \\ 0.980 & 0.067 \end{bmatrix}^{-z} \approx \begin{bmatrix} 0 & 0 \\ 1 & 0 \end{bmatrix}_{ideal}^{-z} \quad (6)$$

The above transmission coefficient values are fairly close to an ideal AT confirming an efficient design. Figure 6 plots the AT parameter extracted from the transmission parameters and assures a magnitude of above 80% in the operating band of interest.

To further characterize the AT performance, Fig. 7 illustrates the total transmission in both directions through the polarization conversion ratio (PCR), that is given as:

$$TotalTransmission = |T_{yx}|^2 + |T_{xx}|^2 \quad (7)$$

$$PCR = \frac{|T_{yx}|^2}{|T_{yx}|^2 + |T_{xx}|^2} = \frac{|T_{yx}|^2}{TotalTransmission} \quad (8)$$

The total transmission for an x-polarized wave in -z-direction remains greater than 80% in the whole range with peaks of 0.938, 0.961 and 0.966 at 6.7, 8.3 and 11.6 GHz, respectively. On the other hand, the transmission remains fairly low in +z-direction. Likewise, the PCR which demonstrates the percentage of transmitted EM wave that undergoes cross-polarization conversion also remains close to unity in a wide operating band as shown in Fig. 7b.

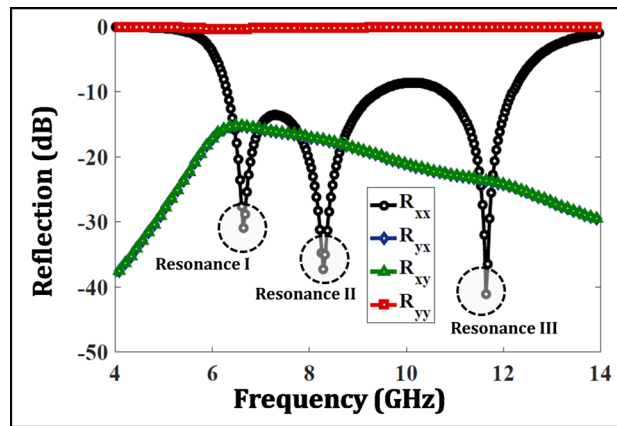


Figure 8. Reflection parameters with identification of three plasmonic resonances.

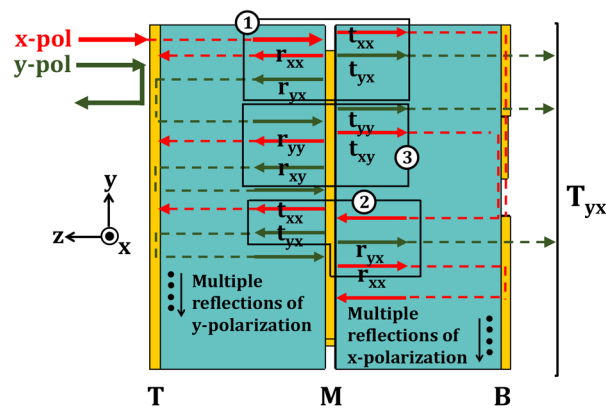


Figure 9. Multiple reflections occurring in multi-layered structure, resembling a Fabry-Perot Cavity.

Asymmetric transmission is a resonant phenomenon and is therefore greatly influenced by reflection parameters of the chiral structure as illustrated in Fig. 8. R_{yy} is around 0dB in the whole range indicating that a y-polarized wave illuminated in $-z$ -direction is significantly reflected. On the other hand, R_{xx} depicts three resonances at 6.6, 8.3 and 11.6 GHz, respectively. The broadband transmission behavior of the metasurface is in fact due to the close proximity of the three plasmonic resonances with one another. In other words, at these resonances, the structure presents a surface impedance to an x-polarized wave which is closer to the free space impedance and therefore results in efficient transmission.

Fabry-perot like resonance in the tri-layered structure. Better understanding of the tri-layered structure can be achieved through Fig. 9. The top and bottom layers (T & B), being similar to orthogonal metallic gratings, act as x and y-polarization selectors. An incident y-polarization in $-z$ -direction suffers reflection while an x-polarized wave is selected by layer T. The x-polarized wave then passes through layer T and moves on to interact with the middle layer (M) which breaks the wave into four parts (t_{xx} , t_{yx} , r_{xx} , r_{yx}) as shown in the labeled region 1. Out of the two transmitted waves t_{yx} is selected by layer B thus contributing towards the resultant y-polarization at the output. t_{xx} , on the other hand, suffers reflection by B and on return also interacts with middle layer to be broken into four parts as shown in region 2. The reflection r_{yx} from region 1 suffers another reflection from the layer T and similarly, is again broken into its constituents by the middle layer (region 3). Continuing the same analysis it can be seen that selectors T and B along with middle layer M cause multiple reflections of y-polarization in the MT region and that of x-polarization in MB region. These multiple reflections resemble a Fabry-Perot cavity⁴⁶ that, in turn, results in enhanced peaks of transmission.

Angular stability of designed metasurface. *Response to oblique incidences.* AT devices, when employed in practical environments should offer robust performance for varying incident angles. In order to analyze this, the transmission response has been plotted against multiple oblique incidences ranging from 0° to 45° in Fig. 10. It is observable that the transmission response maintains a level of greater than 80% against the varying incident angles indicating a robust performance in the whole frequency range of interest. Likewise, the

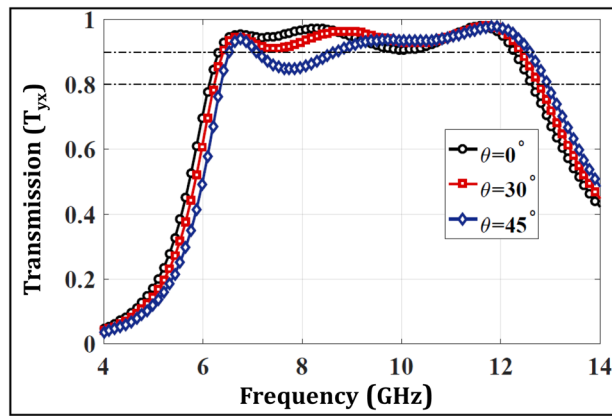


Figure 10. Transmission behavior with respect to different incident angles for proposed structure.

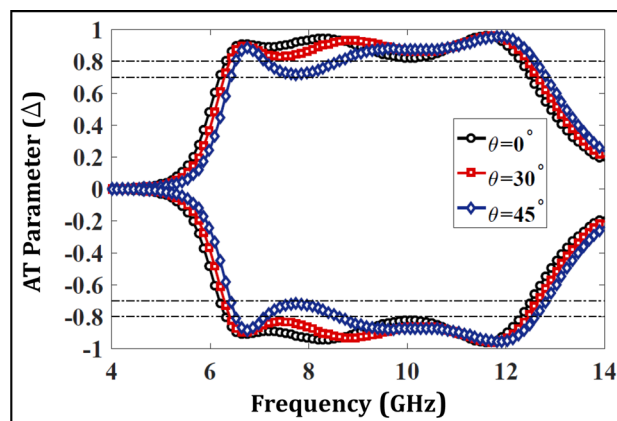


Figure 11. Variation of AT with incident angles for the proposed structure.

AT parameter at the same angles is shown in Fig. 11 that shows a magnitude greater than 70% indicating an angularly stable performance of the proposed AT device.

Surface impedance mismatch at oblique incidences. This subsection provides insights on the dependence of AT phenomenon on the concept of surface impedance mismatch. As the incident angle increases, the resonances in the structure become weaker and result in magnitude drop of transmission with increasing θ . This is in fact caused by the varying surface impedance (Z_0) that is strongly associated with the incident angle. More specifically, for TM (x-polarization), Z_0 is inversely proportional to θ while it is directly proportional in case of TE (y-polarization) as shown in following two equations (4) and (5)⁴⁷:

$$Z_0^{TM} = \eta_0 \cos \theta \tag{9}$$

$$Z_0^{TE} = \frac{\eta_0}{\cos \theta} \tag{10}$$

where, η_0 is the free space impedance.

The role of surface impedance in case of an ideal asymmetric transmission is illustrated in Fig. 12. At normal incidence ($\theta = 0^\circ$), an incident TM wave is fully transmitted as a TE wave, hence the impedance at both the floquet ports of a metasurface is equal to the free space impedance of 377 ohms. However, when the incident angle increases, TM ports suffers a positive mismatch (e.g. $\eta_0 - Z_0 = 377 - 188 = +189\Omega$) while TE ports suffers a negative mismatch (e.g. $\eta_0 - Z_0 = 377 - 754 = -377\Omega$), thus increasing the overall impedance mismatch ($189 - (-377) = 566\Omega$) between the two ports. The increasing mismatch at higher incident angles due to two different ports (TE & TM) inherently makes the magnitude of asymmetric transmission sensitive to oblique incidences and therefore it is challenging to develop an angularly stable AT device.

Avoidance of grating lobes at higher incidence angles. Study of FSS theory reveals that the deterioration in angular performance of a metasurface is caused by interference of secondary main lobes formed at higher angles of incidence^{48,49}. The phenomena of such unwanted beams, better known as grating lobes, occurs when the

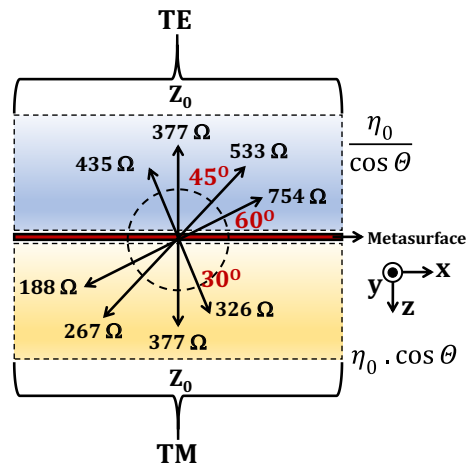


Figure 12. Sensitivity of asymmetric transmission at oblique incidences illustrated through the concept of increasing impedance mismatch at higher angles.

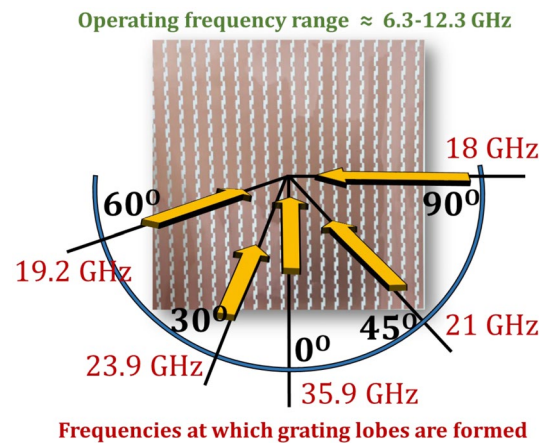


Figure 13. Predicted frequencies of grating lobes.

periodicity (p) of an array becomes electrically large. In order to avoid this, metasurface periodicity should be electrically small in accordance with following relation:

$$p < \frac{\lambda}{1 + \sin \theta} \tag{11}$$

where, λ is the wavelength at highest operating frequency. The required value of p for an angularly stable performance is calculated to be less than 12.1 mm which corresponds to 0.5λ ($p < \frac{24.3\text{mm}}{1 + \sin 90^\circ}$). The periodicity of reported metasurface with $p = 8.3\text{mm}$ (0.3λ) is significantly smaller and hence effectively avoids interference caused by the grating lobes. Furthermore, using the relation given in (7), Fig. 13 depicts the predicted frequencies at which grating lobes are formed against different incident angles.

$$f_{G.L} = \frac{c}{p(1 + \sin \theta)} \tag{12}$$

where, c is the speed of light⁵⁰. It is evident that for all the angles of incidence, grating lobes are formed at frequencies that are far away from the operating band of interest, thus making the reported metasurface angularly stable.

To further clarify the concept, consider a design that functions exactly the same as the reported design i.e. manifesting AT in the frequency range 6.3 to 12.3 GHz, however, its periodicity is larger than 0.5λ e.g. 30 mm. The grating lobes at 30° in this case would form at 6.6 GHz which lies in the operating range and therefore would result in a deteriorated performance at oblique incidences. Thus a miniaturized unit cell is necessary for angular stability. Furthermore, the stability at higher angles of incidence is dependent upon the stability of the resonances in the structure and since AT is a resonant phenomenon, it can therefore be deteriorated if grating lobes are not avoided at higher angles.

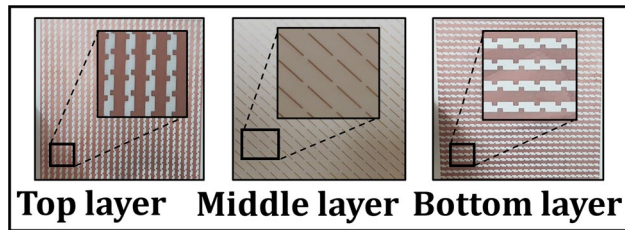


Figure 14. Fabricated prototype of the multi-layered design.

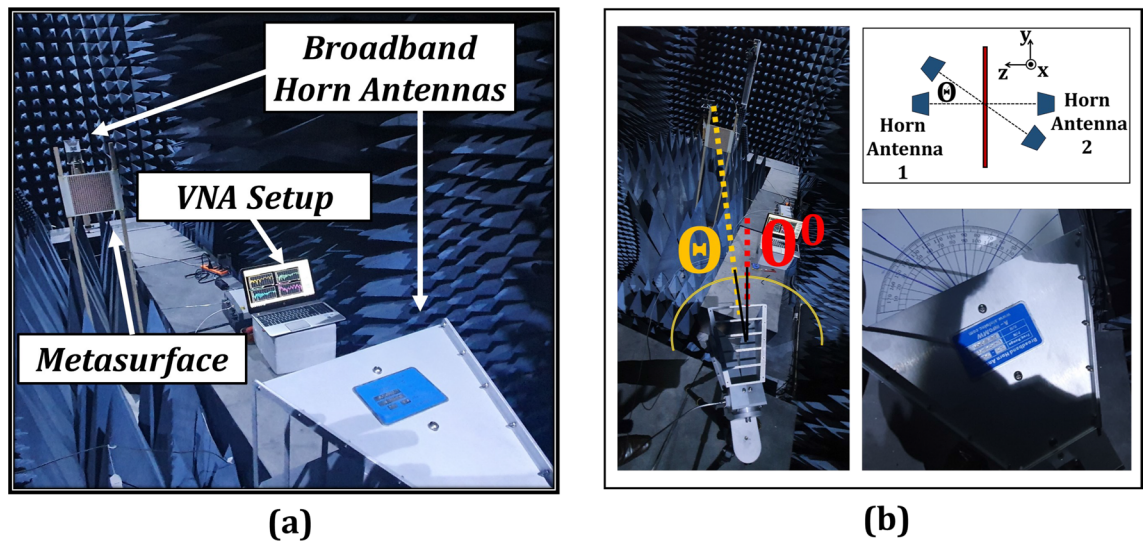


Figure 15. (a) Measurement setup (b) Measurement at oblique incidences.

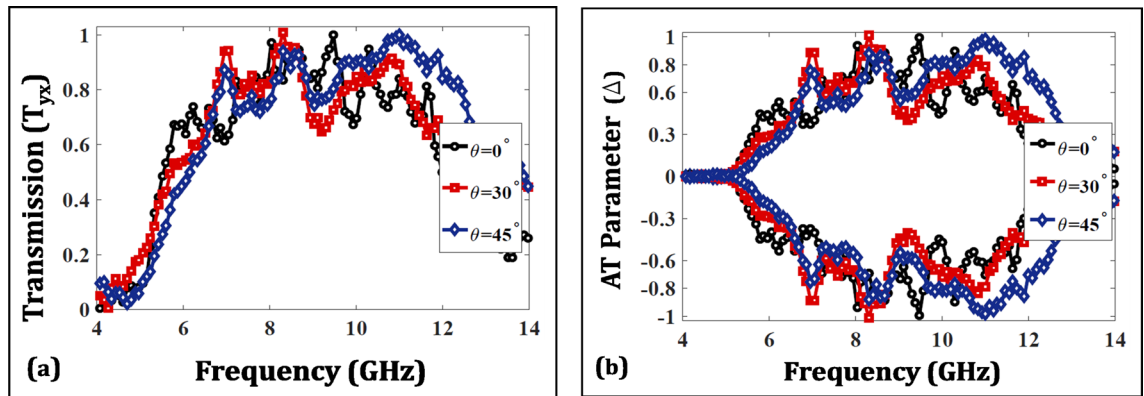


Figure 16. Measured results (a) Transmission parameter (T_{yx}) (b) AT parameter.

Experimental validation. To test the reported multi-layered chiral metasurface, an array of 27×27 unit cells with an electrical size of $7\lambda \times 7\lambda \times 0.07\lambda$ was fabricated using PCB fabrication technology (Fig. 14). The two Rogers substrates were thermally fused using a thin FR4 prepreg. The measurement setup typically consists of two broadband horn antennas with the metasurface between them which are connected to a VNA through coaxial cables as shown in Fig. 15. The antennas are distanced 4 meters from one another to mitigate for the near field effects and Anritsu-MS46122B VNA is used. Moreover, in order to measure the performance at oblique incidences, the antennas were manually rotated around the central axis of metasurface as indicated in Fig. 15(b).

The measured curves for T_{yx} and AT parameter (Δ) for the fabricated prototype are shown in Fig. 16 and show a similar trend to the simulated results. Moreover, the metasurface maintains robustness against oblique incidences ranging from 0° to 45° hence validating an angularly stable performance. The discrepancies from simulations stem from the handling inaccuracies and lack of focusing of EM waves (due to unavailability of dielectric lens). Furthermore, multiple wave reflections also cause fluctuations, which can be minimized using a

Ref	Year	Configuration	Max. BW at normal incidence (AT above 0.8)	Performance at oblique incidences (AT above 0.7)
³²	2018	Bi-layered	15%	30°
³⁵	2020	Bi-layered	2%	60°
³⁶	2020	Tri-layered	3%	40°
³¹	2020	Bi-layered	18%	60°
²¹	2020	Bi-layered	18% approx.	60°
This Work	2021	Tri-layered	64%	45°

Table 1. Comparison with recently published works.

VNA with time gating functionality to monitor the first echo only. A dedicated metasurface measurement setup can further enhance the match between the measurements and simulations.

Discussion

Table 1. shows a comparison of presented metasurface with a few recent works that are relevant in the microwave regime on the merits of operational percentage bandwidth and angular performance³² reports a broadband AT operation that maintains efficiency up to 30°. However, its performance degrades at higher oblique incidences. The designs in³⁵ and³⁶ manifest angular performance up to 60° and 40° in bi-layered and tri-layered configurations, respectively, however, they are limited to a narrow band operation. Furthermore, the recent publication by the authors³¹ although achieves an angularly robust performance up to 60°, however is limited to a bandwidth of 18% that has been improved with a tri-layered variant of the design which ensures a ultra-wide operational bandwidth of 64% with a wide angle performance up to 45°.

Operational bandwidth, in addition to angular stability is a critical parameter for practical applications. Electromagnetic systems are usually prone to two types of variations; spatial variations (related to space e.g. angle of incidence) and temporal variations (related to frequency). Angular robustness of a device caters for the former type of instability while robustness to frequency drift caters for the latter. More importantly, the frequency signals in a practical environment are not necessarily single tones and have a finite bandwidth. To that end, the presented work is robust to frequency variations owing to its wide operating bandwidth of 64%. This feature makes it ideal for practical applications.

In conclusion, the work presented in this report firstly introduces AT operation in analogy with logic gates circuit which may be extended to more complex optical communications systems. The proposed tri-layered chiral metasurface, benefiting from Fabry Perot-like resonances achieves an ultra-broadband operational bandwidth of 64% (6.3 - 12.3 GHz) while maintaining a transmission efficiency of more than 80% and angular stability of up to 45°. Moreover, the susceptibility of AT to higher incident angles is described in terms of surface impedance mismatch between TE and TM ports. Mitigation of grating lobes through design of a miniaturized unit cell is also explained. The performance has been validated through measurements thereby providing designers a complete design methodology to produce angularly robust devices for modern optical communication and radar systems.

Methods

Free space method was used to measure the transmission parameters of the fabricated metasurface that is governed by the following expression:

$$S_{21} = \frac{S_{21}^{\text{metamaterial}} - S_{21}^{\text{MetallicSheet}}}{S_{21}^{\text{airspace}} - S_{21}^{\text{MetallicSheet}}} e^{-jk_0 d} \quad (13)$$

where, measurements are done with a metallic sheet, air and metasurface between the antennas to get $S_{21}^{\text{MetallicSheet}}$, S_{21}^{airspace} and $S_{21}^{\text{metamaterial}}$, respectively⁵¹.

Received: 5 April 2021; Accepted: 19 May 2021

Published online: 03 June 2021

References

- Ning, J. *et al.* Ultra-broadband microwave absorption by ultra-thin metamaterial with stepped structure induced multi-resonances. *Results Phys.* **18**, 103320. <https://doi.org/10.1016/j.rinp.2020.103320> (2020).
- Zhu, B. *et al.* Polarization insensitive metamaterial absorber with wide incident angle. *Progress Electromagn. Res.* **101**, 231–239. <https://doi.org/10.2528/PIER10011110> (2010).
- Zhang, Y., Feng, Y. & Zhao, J. Graphene-enabled active metamaterial for dynamical manipulation of terahertz reflection/transmission/absorption. *Phys. Lett. A* **384**, 126840. <https://doi.org/10.1016/j.physleta.2020.126840> (2020).
- You, X. *et al.* Broadband terahertz transmissive quarter-wave metasurface. *APL Photon.* **5**, 096108. <https://doi.org/10.1063/5.0017830> (2020).
- Zhang, Y. *et al.* Tunable broadband polarization rotator in terahertz frequency based on graphene metamaterial. *Carbon* **133**, <https://doi.org/10.1016/j.carbon.2018.03.038> (2018).
- Ly, T. T. *et al.* Hybrid metamaterial switching for manipulating chirality based on vo2 phase transition. *Sci. Rep.* **6**, 23186. <https://doi.org/10.1038/srep23186> (2016).

7. Akram, M. R., Ding, G., Chen, K., Feng, Y. & Zhu, W. Ultrathin single layer metasurfaces with ultra-wideband operation for both transmission and reflection. *Adv. Mater.* **32**, 1907308. <https://doi.org/10.1002/adma.201907308> (2020).
8. Shadrivov, I. V., Fedotov, V. A., Powell, D. A., Kivshar, Y. S. & Zheludev, N. I. Electromagnetic wave analogue of an electronic diode. *New J. Phys.* **13**, 033025. <https://doi.org/10.1088/1367-2630/13/3/033025> (2011).
9. Kodera, T., Parsa, A. & Caloz, C. Non-reciprocal ferrite antenna radome: The faradome. In *2009 IEEE Antennas and Propagation Society International Symposium*, 1–4. <https://doi.org/10.1109/APS.2009.5171697> (2009).
10. Taravati, S., Khan, B. A., Gupta, S., Achouri, K. & Caloz, C. Nonreciprocal nongyrotropic magnetless metasurface. *IEEE Trans. Antennas Propag.* **65**, 3589–3597. <https://doi.org/10.1109/TAP.2017.2702712> (2017).
11. Fedotov, V. A. *et al.* Asymmetric propagation of electromagnetic waves through a planar chiral structure. *Phys. Rev. Lett.* **97**, 167401. <https://doi.org/10.1103/PhysRevLett.97.167401> (2006).
12. Bokhari, S. H. A. & Cheema, H. M. Broadband asymmetric transmission via angle-induced chirality enhancement in split ring resonators. *J. Appl. Phys.* **128**, 063102. <https://doi.org/10.1063/5.0013033> (2020).
13. Menzel, C. J. *et al.* Asymmetric transmission of linearly polarized light at optical metamaterials. *Phys. Rev. Lett.* **104**, 25, 253902 (2010).
14. Mirzamohammadi, F., Nourinia, J., Ghobadi, C. & Majidzadeh, M. A bi-layered chiral metamaterial with high-performance broadband asymmetric transmission of linearly polarized wave. *AEU Int. J. Electron. Commun.* **98**, 58–67. <https://doi.org/10.1016/j.aeue.2018.11.008> (2019).
15. Liu, D., Xiao, Z. & Wang, Z. Multi-band asymmetric transmission and 90° polarization rotator based on bi-layered metasurface with f-shaped structure. *Plasmonics* **12**, 445–452. <https://doi.org/10.1007/s11468-016-0284-4> (2017).
16. Shi, J. *et al.* Dual-band asymmetric transmission of linear polarization in bilayered chiral metamaterial. *Appl. Phys. Lett.* **102**, 191905. <https://doi.org/10.1063/1.4805075> (2013).
17. Xu, Y., Shi, Q., Zhu, Z. & Shi, J. Mutual conversion and asymmetric transmission of linearly polarized light in bilayered chiral metamaterial. *Opt. Express* **22**, 25679–25688. <https://doi.org/10.1364/OE.22.025679> (2014).
18. Shi, J. H., Ma, H. F., Guan, C. Y., Wang, Z. P. & Cui, T. J. Broadband chirality and asymmetric transmission in ultrathin 90°-twisted babinet-inverted metasurfaces. *Phys. Rev. B* **89**, 165128 (2014).
19. Lai, P. *et al.* Angle enhanced circular dichroism in bilayer 90°-twisted metamaterial. *Opt. Express* **28**, 15071–15080 (2020).
20. Long, F. *et al.* Wideband and high-efficiency planar chiral structure design for asymmetric transmission and linear polarization conversion. *J. Appl. Phys.* **127**, 023104. <https://doi.org/10.1063/1.5129912> (2020).
21. Ullah, T. & Rashid, A. Angularly stable and broadband chiral metamaterial based design for asymmetric transmission of linearly polarized waves. *Microw. Opt. Technol. Lett.* **63**, 226–234. <https://doi.org/10.1002/mop.32564> (2021).
22. Aisha, S., Ismail Khan, M., Chen, Y., Hu, B. & Khan, I. An efficient chiral polarization rotator with asymmetric transmission for large incidence angles. *J. Appl. Phys.* **128**, 213102. <https://doi.org/10.1063/5.0022574> (2020).
23. Liu, M. *et al.* Temperature-controlled asymmetric transmission of electromagnetic waves. *Sci. Rep.* **9**, 4097. <https://doi.org/10.1038/s41598-019-40791-4> (2019).
24. Xu, K.-K., Xiao, Z.-Y., Jingyao, T., Liu, D. & Wang, Z.-H. Ultra-broad band and dual-band highly efficient polarization conversion based on the three-layered chiral structure. *Physica E Low-dimen. Syst. Nanostruct.* **81**, <https://doi.org/10.1016/j.physe.2016.03.015> (2016).
25. Yin Xiao, Z., Jun Liu, D., Long Ma, X. & Hua Wang, Z. Multi-band transmissions of chiral metamaterials based on fabry-perot like resonators. *Opt. Express* **23**, 7053–7061. <https://doi.org/10.1364/OE.23.007053> (2015).
26. Song, K., Liu, Y., Luo, C. & Zhao, X. High-efficiency broadband and multiband cross-polarization conversion using chiral metamaterial. *J. Phys. D Appl. Phys.* **47**, 505104. <https://doi.org/10.1088/0022-3727/47/50/505104> (2014).
27. Jun Liu, D., Yin Xiao, Z., Long Ma, X. & Hua Wang, Z. Broadband asymmetric transmission and multi-band 90° polarization rotator of linearly polarized wave based on multi-layered metamaterial. *Opt. Commun.* **354**, 272–276. <https://doi.org/10.1016/j.optcom.2015.04.043> (2015).
28. Ji, W. *et al.* High-efficiency and ultra-broadband asymmetric transmission metasurface based on topologically coding optimization method. *Opt. Express* **27**, 2844–2854. <https://doi.org/10.1364/OE.27.002844> (2019).
29. Cheng, Y., Zhao, J.-C., Mao, X. & Gong, R. Ultrabroadband diode-like asymmetric transmission and high-efficiency cross-polarization conversion based on composite chiral metamaterial. *Progress Electromagn. Res.* **160**, 89–101. <https://doi.org/10.2528/PIER17091303> (2017).
30. Zhang, L. *et al.* Ultrabroadband design for linear polarization conversion and asymmetric transmission crossing x- and k- band. *Sci. Rep.* **6**, 33826. <https://doi.org/10.1038/srep33826> (2016).
31. Bokhari, S. H. A. & Cheema, H. M. A bilayered, broadband, angularly robust chiral metasurface for asymmetric transmission. *IEEE Antennas Wirel. Propag. Lett.* **20**, 23–27. <https://doi.org/10.1109/LAWP.2020.3037045> (2021).
32. Stephen, L., Yogesh, N. & Subramanian, V. Broadband asymmetric transmission of linearly polarized electromagnetic waves based on chiral metamaterial. *J. Appl. Phys.* **123**, 033103. <https://doi.org/10.1063/1.5008614> (2018).
33. Chen, K. *et al.* Dynamic control of asymmetric electromagnetic wave transmission by active chiral metamaterial. *Sci. Rep.* **7**, 42802. <https://doi.org/10.1038/srep42802> (2017).
34. Liu, D.-Y., Yao, L.-F., Zhai, X.-M., Li, M. & Dong, J.-F. Diode-like asymmetric transmission of circularly polarized waves. *Appl. Phys. A* **116**, 9–13. <https://doi.org/10.1007/s00339-014-8519-8> (2014).
35. Khan, M. I. *et al.* Efficient asymmetric transmission for wide incidence angles using bi-layered chiral metasurface. *J. Phys. D Appl. Phys.*
36. Khan, M. I. *et al.* Multiband efficient asymmetric transmission with polarization conversion using chiral metasurface. *IEEE Antennas Wirel. Propag. Lett.* **1–1**, (2020).
37. Grady, N. K. *et al.* Terahertz metamaterials for linear polarization conversion and anomalous refraction. *Science* **340**, 1304–1307. <https://doi.org/10.1126/science.1235399> (2013).
38. Menzel, C., Rockstuhl, C. & Lederer, F. Advanced jones calculus for the classification of periodic metamaterials. *Phys. Rev. A* **82**, 053811. <https://doi.org/10.1103/PhysRevA.82.053811> (2010).
39. Huang, C., Feng, Y., Zhao, J., Wang, Z. & Jiang, T. Asymmetric electromagnetic wave transmission of linear polarization via polarization conversion through chiral metamaterial structures. *Phys. Rev. B* **85**, 195131. <https://doi.org/10.1103/PhysRevB.85.195131> (2012).
40. Asadchy, V. S., Diaz-Rubio, A. & Tretyakov, S. A. Bianisotropic metasurfaces: physics and applications. *Nanophotonics* **7**, 1069–1094. <https://doi.org/10.1515/nanoph-2017-0132> (2018).
41. Li, Z., Mutlu, M. & Ozbay, E. Chiral metamaterials: from optical activity and negative refractive index to asymmetric transmission. *J. Opt.* **15**, 023001. <https://doi.org/10.1088/2040-8978/15/2/023001> (2013).
42. Jun Liu, D. *et al.* Broadband asymmetric transmission and polarization conversion of a linearly polarized wave based on chiral metamaterial in terahertz region. *Wave Motion* **66**, 1–9. <https://doi.org/10.1016/j.wavemoti.2016.05.003> (2016).
43. Mirzamohammadi, F., Nourinia, J., Ghobadi, C. & Naderali, R. A dual-wideband bi-layered chiral metamaterial to develop cross-polarization conversion and asymmetric transmission functionalities for the linearly polarized electromagnetic waves. *AEU Int. J. Electron. Commun.* **111**, 152916. <https://doi.org/10.1016/j.aeue.2019.152916> (2019).

44. Mutlu, M., Akosman, A. E., Serebryannikov, A. E. & Ozbay, E. Asymmetric transmission of linearly polarized waves and polarization angle dependent wave rotation using a chiral metamaterial. *Opt. Express* **19**, 14290–14299. <https://doi.org/10.1364/OE.19.014290> (2011).
45. Plum, E. *et al.* Metamaterial with negative index due to chirality. *Phys. Rev. B* **79**, 035407. <https://doi.org/10.1103/PhysRevB.79.035407> (2009).
46. Wang, H.-B., Zhou, X., Tang, D.-F. & Dong, J.-F. Diode-like broadband asymmetric transmission of linearly polarized waves based on fabry-perot-like resonators. *J. Mod. Opt.* **64**, 1–10. <https://doi.org/10.1080/09500340.2016.1260778> (2016).
47. Luukkonen, O. *et al.* Simple and accurate analytical model of planar grids and high-impedance surfaces comprising metal strips or patches. *IEEE Trans. Antennas Propag.* **56**, 1624–1632 (2008).
48. Wu, T.-K. *Frequency Selective Surfaces* (American Cancer Society, New York, 2005).
49. Munk, B. A. *Frequency Selective Surfaces: Theory and Design* (John Wiley & Sons Ltd, New York, 2000).
50. Kriezis, E. E. & Chrissoulidis, D. P. Em-wave scattering by an inclined strip grating. *IEEE Trans. Antennas Propag.* **41**, 1473–1480 (1993).
51. Gonçalves, F., Pinto, A., Mesquita, R., Silva, E. & Brancaccio, A. Free-space materials characterization by reflection and transmission measurements using frequency-by-frequency and multi-frequency algorithms. *Electronics* **7**, 260. <https://doi.org/10.3390/electronics7100260> (2018).

Acknowledgements

Authors would like to acknowledge Rogers Corp. for providing free substrate samples. Authors would also like to acknowledge Mubashir Saleem, Mudassir Ali, Ehsanullah Zafar, Muhammad Zeeshan and Tayyab Hassan for their assistance in performing the measurements.

Author contributions

S.H.A.B designed the unit-cell, performed simulations and wrote the manuscript. H.M.C contributed to the concept and wrote the relevant text. H.M.C also supervised the whole research work.

Competing interests

The authors declare no competing interests

Additional information

Correspondence and requests for materials should be addressed to H.M.C.

Reprints and permissions information is available at www.nature.com/reprints.

Publisher's note Springer Nature remains neutral with regard to jurisdictional claims in published maps and institutional affiliations.



Open Access This article is licensed under a Creative Commons Attribution 4.0 International License, which permits use, sharing, adaptation, distribution and reproduction in any medium or format, as long as you give appropriate credit to the original author(s) and the source, provide a link to the Creative Commons licence, and indicate if changes were made. The images or other third party material in this article are included in the article's Creative Commons licence, unless indicated otherwise in a credit line to the material. If material is not included in the article's Creative Commons licence and your intended use is not permitted by statutory regulation or exceeds the permitted use, you will need to obtain permission directly from the copyright holder. To view a copy of this licence, visit <http://creativecommons.org/licenses/by/4.0/>.

© The Author(s) 2021